1 **Post-Glacial Climate Forcing of Surface Processes in the Ganges-**

2 **Brahmaputra River Basin and Implications for Carbon Sequestration**

3

4 Christopher J. Hein (hein@vims.edu)[1,2,*], Valier Galy (vgaly@whoi.edu)[2], Albert Galy

5 (agaly@crpg.cnrs-nancy.fr)[3], Christian France-Lanord (cfl@crpg.cnrs-nancy.fr)[3], Hermann

6 Kudrass (kudrass@gmx.de)[4], Tilmann Schwenk (tschwenk@uni-bremen.de)[5]

7

8

9   [1]*Department of Physical Sciences, Virginia Institute of Marine Science, College of William and*
10 *Mary, Gloucester Point, VA USA*

11 [2]*Department of Marine Chemistry and Geochemistry, Woods Hole Oceanographic Institution,*
12 *Woods Hole, MA USA*

13 [3]*Centre de recherches Pétrographiques et Géochimiques - CRPG CNRS-Université de Lorraine,*
14 *15 rue Notre Dame des Pauvres, 54500 Vandœuvre les Nancy, France*

15 [4]*MARUM - Zentrum für Marine Umweltwissenschaften Universität Bremen Leobener Straße*
16 *28359 Bremen, Germany*

17 [5] *Faculty of Geosciences, University of Bremen, Klagenfurter Str. 2-4, 28359 Bremen, Germany*

18

19 * - corresponding author

20

21 **Abstract**

22   Climate has been proposed to control both the rate of terrestrial silicate weathering and

23 the export rate of associated sediments and terrestrial organic carbon to river-dominated margins

24 – and thus the rate of sequestration of atmospheric CO_2 in the coastal ocean – over glacial-

25 interglacial timescales. Focused on the Ganges-Brahmaputra rivers, this study presents records of

26 post-glacial changes in basin-scale Indian summer monsoon intensity and vegetation

27 composition based on stable hydrogen (δD) and carbon ($\delta^{13}C$) isotopic compositions of terrestrial

28 plant wax compounds preserved in the channel-levee system of the Bengal Fan. It then explores

29 the role of these changes in controlling the provenance and degree of chemical weathering of

30 sediments exported by these rivers, and the potential climate feedbacks through organic-carbon

31 burial in the Bengal Fan. An observed 40‰ shift in δD and a 3–4‰ shift in both bulk organic-

32 carbon and plant-wax $\delta^{13}C$ values between the late glacial and mid-Holocene, followed by a

33 return to more intermediate values during the late Holocene, correlates well with regional post-

34 glacial paleoclimate records. Sediment provenance proxies (Sr, Nd isotopic compositions) reveal

35 that these changes likely coincided with a subtle focusing of erosion on the southern flank of the

36 Himalayan range during periods of greater monsoon strength and enhanced sediment discharge.

37 However, grain-size-normalized organic-carbon concentrations in the Bengal Fan remained

38 constant through time, despite order-of-magnitude level changes in catchment-scale monsoon

39 precipitation and enhanced chemical weathering (recorded as a gradual increase in K/Si* and

40 detrital carbonate content, and decrease in $H2O^+$/Si*, proxies) throughout the study period.

41 These findings demonstrate a partial decoupling of climate change and silicate weathering during

42 the Holocene and that marine organic-carbon sequestration rates primary reflect rates of physical

43 erosion and sediment export as modulated by climatic changes. Together, these results reveal the

44 magnitude of climate changes within the Ganges-Brahmaputra basin following deglaciation and

45 a closer coupling of monsoon strength with OC burial than with silicate weathering on millennial

46 timescales.

47

48 **Keywords:** Indian Monsoon; Bengal Fan; Paleoclimate; Sediment Provenance; Biomarkers;

49 Stable Isotopes

50   **Abbreviations:**

51   B-A: Bølling-Allerød interstadial period (14.7–12.7 ka)

52   BoB: Bay of Bengal

53   FA: fatty acid

54   G-B: Ganges and Brahmaputra

55   H1: Heinrich Event H1 (18–15 ka)

56   HCO: Holocene Climatic Optimum (10–6.5 ka)

57   HHC: High Himalaya Crystalline

58   ISM: Indian Summer Monsoon

59   LG: Late Glacial (24–18 ka)

60   LH: Lesser Himalaya

61   NH: Northern Hemisphere

62   OC: organic carbon

63   SoNG: Swatch of No Ground

64   THB: Trans-Himalayan Batholith

65   TSS: Tethyan Sedimentary Series

66   YD: Younger Dryas (12.9–11.7 ka)

67

68   **1. Introduction**

69   Silicate weathering, carbonate precipitation, and organic carbon (OC) burial in marine

70   sediments, are the main mechanisms for sequestering atmospheric CO_2 over a range of

71   timescales. The efficiency of these processes has long been mechanistically linked to climate, in

72   particular temperature and rainfall, such that increased atmospheric CO_2 sequestration under

73   warm and wet conditions would act as a negative feedback, thereby contributing to global

74   climate regulation. Rivers export silicate weathering products and terrestrial OC to the ocean,

75   while river-dominated margins account for the majority of the global burial flux of OC,

76   illustrating their disproportionate role in the global carbon cycle (Hedges and Oades, 1997). Over

77   glacial-interglacial timescales, climate has been proposed to control the rate of export of

78   terrestrial sediment and OC to these depocenters (Ludwig et al., 1998; Galy et al., 2015), as well

79   as rates of chemical weathering, which exert a primary control on carbon sequestration (*e.g.*,

80   West et al., 2005). Heretofore, few studies of large (continental-scale) systems have directly

81   quantified in an integrated manner how past climate change has impacted the basin-scale

82   weathering degree of silicate minerals exported to the coastal ocean, or the competency of those

83   systems to export and bury OC, let alone both.

84   The Ganges and Brahmaputra (G-B) rivers, which drain the vast majority of the

85   Himalayan range and Southern Tibet (Fig. 1a), convey the world's largest fluvial sediment load

86   to the Bay of Bengal (BoB), resulting in the deposition of the world's largest delta (Kuehl et al.,

87   2005) and the world's largest reservoir of terrigenous sediments (~2.9 x 10^{16} tons; Curray et al.,

88   2003). Despite the generally low OC concentration in G-B sediments (typically < 1%), the G-B

89   rivers are currently the largest single supplier of biospheric OC to the world's oceans (Galy et al.,

90   2015). Coupled with excellent OC preservation in Bengal Fan sediments (Galy et al., 2007) and

91   modest silicate weathering rates in the G-B basin (Galy and France-Lanord, 1999), this makes

92   OC burial the leading carbon sequestration mechanism in the G-B system at short (~1000 years)

93   through long (~10 million years) timescales (France-Lanord and Derry, 1997; Galy et al., 2007).

94   Changes in Himalayan erosion driven by climate variability over the last 20 kyr are thus

95   expected to have played a role in the global carbon cycle — specifically the magnitude of carbon

96 sequestration — following the last glacial maximum (21–19 ka). Here, we use a sediment record

97 from the Bengal Fan following the last glacial maximum to 1) reconstruct hydroclimate

98 variability (*i.e.,* monsoon intensity) and attendant paleovegetation changes in the G-B basin and,

99 2) evaluate how these variations in monsoon strength have affected weathering processes as well

100 as sediment and carbon export (and burial) within the G-B basin / Bengal Fan system.

101

102 **2. Regional Setting**

103 *2.1. The Indian Summer Monsoon as a driver of sediment and carbon export to the Bay of*

104 *Bengal*

105   Water and sediment discharge from the G-B rivers are largely controlled by intense

106 precipitation associated with the Indian Summer Monsoon (ISM), a coupled ocean-atmosphere-

107 land climate system driven by cross-equatorial pressure gradients and amplified by land-sea

108 thermal gradients and resulting low-level advection of warm, moisture-laden air from the Indian

109 Ocean (Wu et al., 2012) and insulation of these air masses from the extratropics by the

110 Himalayas (Boos and Kuang, 2010). This generates intense precipitation over western India, the

111 BoB and the southern flank of the Himalayas during the height of the boreal summer. The ISM

112 contributes precipitation that is relatively depleted in deuterium (commonly by >50 ‰) as

113 compared with non-monsoon precipitation (IAEA/WHO, 2016), and accounts for a combined G-

114 B water discharge of *ca.* 1.7 x 10^5 m^3/s, from a boreal winter base level of ~0.2 x 10^5 m^3/s (Sinha

115 et al., 2008)

116

117 *2.2. Sediment and carbon burial in the Bay of Bengal*

118   The primary depocenter of the G-B rivers is the Bengal Fan, the largest submarine fan in

119   the world: it is 832–1430 km wide, extends offshore for *ca.* 3000 km, and its post-Paleocene

120   deposits are up to ~16.5 km thick (Curray et al., 2003). Sediment and OC discharged from G-B

121   rivers are transported by freshwater fluxes through the intertidal delta and further dispersed by

122   tidal currents and storm-induced waves (Kuehl et al., 1997). However, for at least the last

123   125,000 years, the primary conduit for the transfer of large volumes of sediment to the distal fan

124   has been the Swatch of No Ground (SoNG), a 160-km-long deep submarine canyon that

125   penetrates well onto the continental shelf and intercepts westward shelf sediment transport (Fig.

126   2a) (Curray et al., 2003; Kuehl et al., 1997).

127   The upper SoNG serves as a temporary (decades to centuries) storage site for sediment in

128   the Bengal Fan. Triggered by earthquakes, mass wasting and resulting turbidity currents within

129   the SoNG convey large volumes of sediment to the middle and lower Bengal Fan through lateral

130   sheet flow (sand-dominated) and channel overflow (turbidites) via a non-bifurcating, 2500-km

131   long, 13-km-wide, 50-m-thick channel-levee system dominated by 5–35-cm thick sand and mud

132   turbidites (Fig. 2; Curray et al., 2003; Schwenk et al., 2003; Weber et al., 1997).

133

134   **3. Materials and Methods**

135   ***3.1. Sediment core sampling***

136   Three gravity piston cores were retrieved in 2540–2610 m water depth along the middle

137   fan channel-levee system (Fig. 2) during the February 1994 (Expedition SO93) cruise of the R/V

138   SONNE (Weber et al., 1997), coincident with sediment echosounder data (see supplemental

139   materials for details). Core SO93-117KL (~12 m long) was collected from the outer levee. Core

140   SO93-120KL (~11.5 m long) was collected further from the channel; the presence of a small

141   onlap-fill basin suggests that turbidites in this core were not overspilled along the profile shown

142   in Fig. 2b, but are rather from a more northward direction. In contrast, Core SO93-118KL (~8 m

143   long) was collected from a terrace on top of filled cut-off lops proximal to the recent channel

144   pathway (Fig. 2b).

145   The sedimentary stack presented by the three cores consists of alternating turbiditic

146   sequences and rare thin hemipelagic layers; the latter were omitted in this study. Thirty-one

147   samples (1–10 cm thick each) were collected for analysis (Supplemental Table 2). All samples

148   were freeze-dried and homogenized, and aliquots collected for bulk inorganic and organic

149   analyses, with the remainder (>90%) set aside for lipid extraction.

150

151   *3.2. Age models*

152   Age models are based on re-calibration of six reported radiocarbon ($\Delta^{14}C$) ages derived

153   from planktonic foraminifera (*Globigerinoides* sacculifer; Weber et al., 1997) and AMS-

154   radiocarbon dating of planktonic foraminifera (*Globigerinoides* sacculifer, *Globigerinoides*

155   ruber) from 18 additional sedimentary units (Supplemental Table 1). Age models were calculated

156   in the Bayesian age-depth modeling software package Clam 2.1 (Blaauw, 2010), with

157   extrapolation to core bottoms (Fig. 3).

158

159   *3.3. Bulk sediment inorganic and organic analyses*

160   Major and trace element concentrations were determined at SARM (CNRS, Nancy,

161   France) by IPC-AES and ICP-MS and Nd and Sr isotopic compositions at CRPG (Nancy,

162   France) by TIMS and MC-ICPMS, respectively (see supplemental materials). We combine our

163   Sr/Nd data with those from these same sediment cores previously published in Pierson-

164 Wickmann et al. (2001), Galy et al. (2008a), and Lupker et al. (2013) to generate a record of

165 sediment provenance variations at sub-millennial resolution (n=41 over 17.5 kyrs). However, due

166 to methodological bias (see supplemental text), Nd isotopic data from Galy et al. (2008a) and

167 Lupker et al. (2013) are excluded from further analyses.

168   The bulk-sediment weight-percent total-organic-carbon content (TOC) and total-nitrogen

169 content (TN), and stable isotopic composition of bulk organic carbon ($\delta^{13}C_{TOC}$) and nitrogen

170 ($\delta^{15}N_{TN}$), were analyzed for all samples (see supplemental materials for details). These data

171 supplement existing TOC, TN, and $\delta^{13}C_{TOC}$ data from the same cores presented by Galy et al.

172 (2008a).

173

174 *3.4. Compound-specific organic analyses*

175   Lipids were extracted from sample aliquots. Fatty acids (FA) were isolated and

176 methylated using methanol (MeOH) of known D/H (δD) and $\delta^{13}C$ composition. The resulting

177 fatty acid methyl esters (FAMEs) were further purified and quantified, and the $\delta^{13}C$ and δD

178 compositions of individual homologs were measured and mass-balance corrected for the

179 contribution of one additional carbon, and three additional hydrogen atoms per homolog during

180 methylation. Fatty acid δD values (δD_{FA}) were further corrected for variations in seawater

181 isotope composition related to global ice volume variations during the deglaciation (Clark et al.,

182 2009). The resulting ice-volume-corrected FA δD values (δD_{FA-IV}) were then corrected for

183 variable H isotope fractionation by each C3 and C4 vegetation endmembers to estimate

184 precipitation δD values (δD_P) (see supplemental materials for details). This approach carries

185 significant uncertainties (on the order of ± 15 ‰) due to the lack of adequate characterization in

186 the G-B basin of: 1) H isotopic fractionation by the vegetation; and 2) the carbon stable-isotopic

187   composition of the C3 and C4 plants endmembers. Nonetheless, the core-top calculated δD_P

188   value is consistent with modern isotope composition of rainfall in the floodplain/delta

189   (IAEA/WHO, 2016) – the dominant source of plant-wax in G-B river sediments (Galy et al.

190   2008b) – suggesting that the fractionation factors and endmember composition we used are

191   adequate.

192

193   **4. Results**

194   Results of bulk and compound-specific $\delta^{13}C$, $\delta^{15}N$, and δD values are given in

195   Supplemental Table 2. All are reported in ‰ notation against the Vienna Pee Dee Belemnite

196   (VPDB), air, and Vienna Standard Mean Ocean Water (VSMOW) standards, respectively.

197   Measured major and trace inorganic elemental compositions and Sr (given as $^{87}Sr/^{86}Sr$) and Nd

198   (given as εNd) isotopic compositions of bulk sediment samples are given in Supplemental Table

199   3.

200

201   *4.1. Channel-levee core accretion rates: Core age models*

202   Linearized sediment accumulation rates range from <50 to >500 cm/kyr for the three

203   cores. We recognize the obvious limitation of calculating linear rates in turbiditic deposits:

204   sedimentation is episodic in nature, and therefore accumulation rates are largely controlled by

205   mass wasting processes at the turbidite source (*i.e.*, the SoNG) as well as local hydrodynamic

206   conditions at the depocenter.

207   Outer-levee cores SO93-117KL and SO93-120KL (Fig. 2b) record 16.9 and 17.5 kyrs of

208   deposition, respectively, with long-term accumulation rates of 66–72 cm/kyr. Core SO93-120KL

209   also shows significant peaks in sediment deposition *ca.* 10 ka (likely also evident in SO93-

210   117KL) and 12.8–13.6 ka (Fig. 3d); average sediment accretion at 10.2–12.8 ka was 190 cm/kyr.

211   Following the second sediment pulse, sedimentation rates in both outer levee cores fell to among

212   their lowest values (20–60 cm/kyr) for the remainder of the Holocene. These accumulation rates

213   were greatly exceeded by those within the inner levee, where time-averaged Holocene

214   accumulation rates in core SO93-118KL, capturing 9.6 ka to present, were ~120 cm/kyr.

215

216   *4.2. Inorganic elemental and isotopic compositions*

217   Given the turbiditic nature of sediment deposition in the BoB channel levee, grain-size

218   variations are expected to exhibit a first-order control on temporal organic (*e.g.*, OC

219   concentrations) and inorganic (*e.g.*, weathering) records. Al/Si ratios provide a proxy for

220   mineralogical composition and grain size and can be used to correct mobile-to-immobile (*e.g.*,

221   K/Si) ratios for sorting effects to provide (*e.g.*, as K/Si* [grain-size-corrected Si]) a temporal

222   record of chemical weathering (Lupker et al., 2013). Al/Si ratios vary from 0.26 ("coarsest" and

223   most quartz-rich) to 0.46 ("finest" and most phyllosilicate-rich), with most ratios >0.35 (n=64;

224   total n=74), reflecting an intentional sampling bias towards the (fine) top of turbidites. K/Si*

225   ratios — combined with published data (Lupker et al., 2013) replotted with updated core age

226   models — show a progressive decrease through time, from ~0.056 at the LG to ~0.051 at present

227   (2σ standard error on K/Si* is ± 0.0010; Fig. 4a). Likewise, Ca/Si ratios closely correspond to

228   detrital carbonate content (supplemental fig. 5) and are interpreted as a basin-scale weathering

229   proxy by Lupker et al. (2013); these too show a decrease across the deglaciation, from 0.073 at

230   the LG to 0.027 in the late Holocene (Fig. 4b). A notable Ca/Si outlier at 3.7 ka (Ca/Si=0.10;

231   omitted from Fig. 4b) is biased by marine carbonate (8.4% marine carbonate content; average for

232   all samples is 1.2%; sample also has high Sr and Ba concentrations, low C/N ratio, highest $\delta^{15}N$

233 value) and as such does not reflect continental chemical weathering. Together, K/Si* and Ca/Si

234 records reveal an increase in weathering of sediments exported by the G-B rivers across

235 deglaciation; however, this may be partially influenced by changes in sediment provenance. We

236 also note a conspicuous lack of variation in sediment weathering proxies (including H_2O^+/Si*;

237 Supplemental Table 3) in the last 4000 years.

238   Our data demonstrate coherent temporal shifts in both $^{87}Sr/^{86}Sr$ and εNd compositions.

239 Specifically, $^{87}Sr/^{86}Sr$ ratios increase from 0.73–0.74 during the late glacial to 0.75–0.76 by the

240 early Holocene, followed by a gradual return to intermediate values towards present (Fig. 4c).

241 Temporal trends in Nd isotope composition generally inversely follow trends in $^{87}Sr/^{86}Sr$ values

242 ($^{87}Sr/^{86}Sr$ ratios and εNd values are generally negatively correlated) and demonstrate a general

243 shift towards lower εNd values through time (Fig. 4d), with noticeably higher-than-average εNd

244 values immediately following Heinrich Event 1 (H1) (n=3). The chemical composition (chiefly

245 low K/Si* and high εNd values) of these three H1 samples is unusual compared to the rest of the

246 dataset, suggesting they have a significant hemipelagic component more influenced by

247 sedimentary supply from the Burmese Range in the BoB (*e.g.*, Colin et al., 2006; Joussain et al.,

248 2016; Supplemental Fig. 6).

249

250 **4.3. Bulk organic properties and lipid distributions**

251   TOC and TN values, both of which are similarly dependent on sediment surface area,

252 range from 0.4% to 0.8% (average: 0.6%) and 0.047% to 0.10% (average: 0.07%), respectively;

253 these are weakly correlated (Supplemental Fig. 7). Resulting TOC:TN ratios range from 8.6 to

254 11.7 and show a small, gradual decrease through time; an anomalous high value (TOC:TN =

255 15.5) corresponds with the period of highest outer-levee sedimentation at 10.2–10.3 ka (Fig. 5a).

256   TOC values are highly sensitive to sediment grain size and bulk mineral composition

257   (Galy et al., 2007; 2008a) and are thus normalized to sediment Al/Si. Carbon loading (OC*) –

258   the deviation in TOC for a given sample from the linear trend between modern Lower Meghna

259   River sediment TOC and Al/Si values (see Galy et al., [2007, 2008b]) – was calculated

260   independently for new samples and for those from Galy et al. (2008a) due to methodological

261   differences (see supplemental materials and Supplemental Figs 2, 3, 4). The resulting values are

262   discussed as relative deviations (expressed in %) with respect to modern OC loading of the

263   Lower Meghna River, the combined outflow of the G-B rivers (Fig. 5b).

264   Channel-levee OC* values show no temporal trend. Mean OC* over the entire time

265   period is -1% of modern mean Lower Meghna River sediments OC loading. Excluding outliers

266   of +103%, +74%, and +58% at 8.6, 11.7, and 15.8 ka, respectively (the latter of these – the only

267   for which we have Nd isotopic data – coincides with a H1 hemipelagic sample), all channel-

268   levee OC* values are well within variability of the modern river system, and within 35% of

269   mean Lower Meghna sediments (Fig. 5b). Together, these data imply that, over the last 18 kyr,

270   the carbon loading of sediments deposited in the channel-levee system is, on average,

271   statistically identical to the modern river.

272

273   ***4.4. Paleo-vegetation and paleo-hydrology: Bulk $\delta^{13}C$ and fatty acid $\delta^{13}C$ and δD compositions***

274   Relatively small differences in isotopic composition were observed among long-chain

275   homologs (see Supplementary Table 1). C_{28} FA, which was consistently the most abundant

276   homolog (average concentration: 0.64 μg/g), and weighted-average C_{24-32} FA are the focus of

277   discussion.

278   Bulk $\delta^{13}C_{org}$ values (this study and Galy et al., 2008a, re-plotted with the updated age

279   model) record a 3–4‰ decrease between the LG and the Holocene climatic optimum (HCO),

280   followed by a gradual return to more intermediate values (*ca.* -20.5‰) during the last 8 kyr (Fig.

281   6a). C_{28} FA and weighted-average C_{24-32} FA $\delta^{13}C$ values demonstrate similar temporal trends.

282   Between 8 ka and present, $\delta^{13}C$ values for both C_{24-32} and C_{28} FA increased by *ca.* 1.6‰ (Fig.

283   6b). Weighted-average C_{24-32} and C_{28} FA $\delta^{13}C$ and $\delta^{13}C_{org}$ values were anomalously depleted (-

284   30.0‰, -29.5‰, and -21.3‰, respectively) at 13.7 ka (Bølling-Allerød). All FA homologs from

285   this sample were similarly depleted.

286   Ice-volume-corrected C_{24-32} δD_{FA-IV} and C_{28} δD_{FA-IV} increase by ~15‰ in the 2000 years

287   following the LG, followed by a *ca.* 40‰ decrease until the HCO, and then a return towards

288   more intermediate values of -160 to -170‰ (similar to those representatives of the early

289   Holocene) between the HCO and present (Fig. 7). δD_{FA-IV} values for both C_{24-32} FA and C_{28} FA

290   are within error through most of the record. However, they diverge in the middle to late

291   Holocene (between *ca.* 6500 and 2500 BP), a trend largely driven by a higher degree of depletion

292   of C_{28} FA (~9–13‰) as compared to C_{24}, C_{26}, C_{30}, and C_{32} homologs. Both C_{24-32} and C_{28} FA δD

293   values for a single sample at 12.7 ka (Younger Dryas) are enriched by ~20‰ with respect to

294   samples from similar time periods (Figs. 7a,b); all individual FA homologs for this time period

295   are similarly enriched.

296   Precipitation D/H values (δD_P) calculated from measured C_{24-32} and C_{28} FA, corrected for

297   ice-volume and vegetation effects, increase by ~30‰ (decrease in humidity) in the 2000 years

298   following the LG (Fig. 7c). This was followed by a gradual, ~50‰, depletion in δD values

299   between 16 ka and the HCO (10–6.5 ka), consistent with increased ISM intensity. However, this

300   trend contains substantial internal variability, with a negative excursion of 23–27‰ at 13.7 ka

13

301   and a positive excursion of 27–30 ‰ at 12.7 ka, corresponding with the Bølling-Allerød and

302   Younger Dryas, respectively. Calculated δD_P values from the youngest samples, corresponding

303   to the last 500 years, range from -30 to -40‰. These values compare favorably to measured

304   precipitation δD values from the Indo-Gangetic floodplain and the G-B delta in Bangladesh (see

305   supplemental materials). With single $\delta^{13}C$ (13.6 ka; Bølling-Allerød) and δD (12.7 ka; Younger

306   Dryas) outliers removed, there is a strong positive correlation between δD_P and $\delta^{13}C$ values of

307   both $C_{24\text{-}32}$ (R^2=0.72) and C_{28} (R^2=0.67) FA (Fig. 8).

308

309   **5. Discussion**

310   ***5.1. Records of monsoon intensity and vegetation change within the G-B Basin since the Late***

311   ***Glacial***

312   Floodplain sediment and organic matter – and associated provenance and paleoclimate

313   and paleovegetation signatures – exported from the G-B river basin are transferred to the BoB

314   depositional system on sub-millennial timescales (Galy and Eglinton, 2011; Galy et al., 2011;

315   Lupker et al., 2012, 2013). However, $\delta^{13}C$ measurements of $C_{24\text{-}32}$ FA and *n*-alkanes extracted

316   from G-B river sediments reveal that modern OC is subject to extensive turnover and

317   replacement during transit through the floodplain. This is manifested as a downstream increase in

318    $\delta^{13}C$ values, indicating partial degradation and replacement of the C3 vegetation signal

319   emanating from Himalayan rivers by OC from mixed C3/C4 vegetation in the floodplain (Galy et

320   al., 2011). Thus, environmental signatures encoded in the stable isotopic composition of plant

321   biomarkers within the BoB channel levee system, at least at present, primarily reflect the

322   floodplain environment.

323   Nonetheless, there remains a close synchronicity between records derived from mid-fan

324   BoB archives and regional terrestrial climate reconstructions (*e.g.*, Galy et al., 2008a; Lupker et

325   al., 2013). Likewise, our terrestrial leaf-wax paleo-precipitation (Fig. 9f) and paleo-vegetation

326   (Fig. 9l,m) proxy records display many of the same temporal trends observed in independent

327   proxy records of the ISM, such as those from terrestrial speleothems (Fig. 9a; Cheng et al.,

328   2016), marine foraminifera (Fig. 9c; Weber et al., 1997; Galy et al., 2008a), and reconstructions

329   of salinity in the northern BoB (Fig. 9d; Kudrass et al., 2001). Specifically, our leaf-wax δD and

330    $\delta^{13}C$ records document millennial-scale climate events (*e.g.*, H1, Bølling-Allerød, and Younger

331   Dryas) as well as longer-term, orbitally-driven climate trends; these changes, and underlying

332   mechanisms, are discussed in detail in the following sections.

333

334   *5.1.1. Post-glacial changes in monsoon strength in the Ganges-Brahmaputra Basin*

335   Changes in Northern Hemisphere (NH) summer insolation control ISM strength on

336   orbital and sub-orbital timescales (*e.g.*, Cheng et al., 2016; Clement et al., 2001). Over shorter

337   periods, variations in ISM strength have also been explained by changes in tropical sea surface

338   temperatures, changes in Eurasian snow cover, and linkages with the El Niño–Southern

339   Oscillation (*e.g.*, Vernekar et al., 1995). During the LG, reduced differential heating between the

340   Indian Ocean and the Asian continent weakened summer circulation and produced cooler, drier

341   conditions over Asia and across the Himalayas (Clement et al., 2001). Strengthening NH

342   insolation during deglaciation and until the Holocene Climatic Optimum (9–5 ka) corresponded

343   with a general increase in monsoonal activity and an increase in mean effective moisture over

344   central Asia and in the G-B basin (Fig. 9b; Herzschuh, 2006). These variations were manifested

345   as a general decrease in northern BoB salinity (Fig. 9c,d; Kudrass et al., 2001). These trends

15

346   have reversed as ISM strength has weakened since the mid-Holocene in response to primarily

347   precession-driven declining NH summer insolation (Rao et al., 2016).

348   Over multi-annual timescales, terrestrial leaf-wax δD reconstructions have been

349   demonstrated to respond to changes in precipitation amount (rather than moisture source) in the

350   G-B basin (Contreras-Rosales et al., 2014; Rao et al., 2016). These trends are confirmed by leaf-

351   wax proxy records presented here (Fig. 9f) and by those recently published from a sediment core

352   on the northern BoB slope (SO188-342KL, see location, Fig. 2a) (Contreras-Rosales et al., 2014;

353   Fig. 9e). Close temporal correlation of BoB leaf-wax records with independent proximal

354   terrestrial and marine climate reconstructions (although there remains a disconnect with records

355   of Arabian Sea wind variability; see, *e.g.*, Clemens et al. [2010]) indicates high sensitivity of the

356   G-B basin and these leaf-wax proxies to changes in ISM strength during the period following the

357   LG, and confirm earlier observations of broad regional coherence in ISM variability (Fig. 9). For

358   example, δD_{FA-IV} (this study) and δD_{alk-IV} (Contreras-Rosales et al., 2014) reconstructions during

359   the LG through H1 show a gradual enrichment (weakening ISM) corresponding with early stages

360   of enhancement of NH summer insolation (Fig. 9e,f). This is a recognized feature of ISM

361   response to the collapse of NH ice sheets: the release of cold ice and meltwater into the North

362   Atlantic propagates through the ocean and atmosphere, reducing regional relative humidity and

363   temporally weakening the ISM (Cheng et al., 2016).

364   Quantitatively, our calculated δD_P values from the post-LG period, and in particular H1

365   event (-7‰), are suggestive of very weak summer monsoon. The modern, multidecadal δD_P

366   time-series from New Delhi (IAEA/WMO, 2016) shows that such enriched δD_P values are

367   currently mainly restricted to outside the summer monsoon season (*i.e.*, during the "dry" period).

368   These New Delhi data do not show a clear dependence of δD_P to the annual or monthly

16

369   precipitation amount (*i.e.*, an amount effect as per Dansgaard's definition). However, a mixing of

370   water masses characterized by drastically different isotope composition (δD_P, but also deuterium

371   excess) is evident, with the summer monsoon period overall characterized by highly depleted

372   isotope compositions (and high precipitation amount). If these observations can be transposed to

373   past hydroclimate conditions, our calculated δD_P value for the H1 event requires a reduction in

374   the amount of summer monsoon rainfall by an order of magnitude as compared to the modern

375   period (>80% of annual precipitation), resulting in muted seasonality, and a ~3x reduction in

376   annual precipitation amount (assuming inter-monsoon precipitation levels remained at modern

377   levels). Such diminished precipitation is consistent with the lack of significant freshwater

378   dilution suggested by estimates of BoB seawater salinity at the LG/H1 (Kudrass et al., 2001;

379   Marzin et al., 2013; Fig. 9d), and is in line with the rare modern occurrence of very weak

380   monsoons (total annual precipitation <500 mm in five of 39 years) in New Delhi, which result in

381   much lower-than-normal seasonality and annual rainfall, and enriched annually averaged δD_P

382   values (IAEA/WMO, 2016).

383   Our results continue to match regional ISM reconstructions well throughout the early

384   through middle Holocene (see, *e.g.*, Rao et al., 2016 and references therein), demonstrating a

385   period of higher humidity (more depleted δD_P values) during the early to early-middle Holocene,

386   and gradually returning to more intermediate values during the last 6000 years.

387   In contrast, neither our, nor earlier (Contreras-Rosales et al., 2014), leaf-wax δD records

388   capture the anomalous (with respect to decreasing NH summer insolation), subtle increase in

389   monsoon strength during the past 2000 years observed in Chinese cave $\delta^{18}O$ records (Fig. 9a;

390   Cheng et al., 2016; Rao et al., 2016); this same shift was also not observed in atmospheric O_2

391   $\delta^{18}O$ records (Severinghaus et al., 2009). This may indicate that the recent increase in monsoon

392   strength recorded in Chinese cave records is a feature of the greater amount-effect sensitivity of

393   these sites to more subtle changes in monsoon strength due to their higher elevations and more

394   distal locations with respect to moisture source (Botsyun et al., 2016).

395

396   *5.1.2. Post-glacial changes in vegetation dominance in the Ganges-Brahmaputra Basin*

397   Comparison of modern river sediments with those buried in the Bengal Fan channel-levee

398   system revealed that grain-size-normalized OC concentrations remain constant from the fluvial

399   to the marine environment and that, during deposition and burial in the modern fan, the input of

400   marine organic matter is muted by the very large influx of terrestrial matter (Galy et al., 2007,

401   2008b). New bulk and compound-specific $\delta^{13}C$ records demonstrate a remarkable positive

402   correlation (R^2=0.84) (Fig. 8a). Moreover, there is a lack of a systematic variation in leaf-wax

403   contributions to the OC pool since the LG (Fig. 5c). Together, these observations confirm that

404   the strong predominance of terrestrially-derived organic matter in BoB channel-levee sediments

405   has persisted for at least the last 18 kyr.

406   Paleo-vegetation data (this study and Galy et al., 2008a; Fig. 9l) demonstrate a 3–4 ‰

407   shift in $\delta^{13}C_{org}$ between H1 and the HCO, recognized as a transition of terrestrial vegetation from

408   dominantly C4, savanna-like, to dominantly C3, forest-like, in response to increased atmospheric

409   CO_2 concentrations and decreased water stress (Galy et al., 2008a). This was followed by a

410   gradual return to more intermediate values (*ca.* -20.5‰) during the last 8 kyr. These same trends

411   are also captured in compound-specific $\delta^{13}C_{FA}$ records (Fig. 9m). The relative enrichment (C4-

412   like signal) of both $\delta^{13}C_{org}$ and $\delta^{13}C_{FA}$ throughout the period of study (as compared to a pure C3

413   Himalayan signature [modern C_{24-32} FA $\delta^{13}C$ at base of Himalayas: min = -32.5‰; max = -

414   30.8‰]; Galy et al., 2011) suggest that the role of OC turnover and replacement by floodplain

415   vegetation is a long-standing feature of this system. This observation may also explain the outlier

416   sample corresponding with the Bølling-Allerød at 13.6 ka, which has a strongly depleted $\delta^{13}C_{FA}$

417   and somewhat depleted δD_P signal, possibly suggesting an excess Himalayan OC input at this

418   time; this is further supported by sediment provenance data (see section 5.2). We posit that this

419   sample may capture a short-lived period of rapid and direct (*i.e.*, without time for floodplain

420   organic matter turnover) discharge of sediment and OC from the upper Brahmaputra basin

421   associated with megaflood discharge on the Tsangpo River, similar to other well-documented

422   episodes during this time (*e.g.*, Huang et al., 2014).

423   There is close correspondence between C3/C4 vegetation composition as reflected in

424    $\delta^{13}C_{FA}$ values and precipitation isotope composition as reflected in δD_{FA-IV} records (Fig. 8b).

425   This correlation reflects the combined effect of precipitation regime changes driving a

426   corresponding change in vegetation type, and the differential fractionation of stable hydrogen

427   isotopes by different photosynthetic pathways of each C3 and C4 vegetation; derivation of δD_P

428   attempts to remove some of the latter factor. Comparison of $\delta^{13}C_{FA}$ (Fig. 9m) and δD_P (Fig. 9f)

429   records reveals close temporal correspondence; that is, there is a relatively rapid (centennial or

430   shorter) response of vegetation composition to hydroclimate changes.

431

432   ***5.2. Concurrent Himalayan Climatic and Sediment Provenance Shifts since the Late Glacial***

433   The lithological diversity of the G-B basin is reflected in markedly different Sr and Nd

434   isotopic signatures of source rocks in its major geological terranes (Fig. 1b). Modern G-B

435   sediment is dominated by mixing between four primary sources: (1) Trans-Himalayan Batholith

436   (THB), with relatively high εNd values (*ca.* -5 to -8) and low $^{87}Sr/^{86}Sr$ ratios (*ca.* 0.70–0.72); (2)

437   Tethyan Sedimentary Series (TSS), with lower εNd values (*ca.* -10 to -17) and higher $^{87}Sr/^{86}Sr$

438   ratios (*ca.* 0.72–0.73); (3) Lesser Himalaya (LH), with low εNd values (*ca.* -22 to -28) and high

439   ^{87}Sr/^{86}Sr ratios (*ca.* 0.81–0.92); and (4) High Himalaya Crystalline (HHC) (εNd: -12 to -17;

440   ^{87}Sr/^{86}Sr: 0.73–0.77), whose intermediate ^{87}Sr/^{86}Sr and εNd compositions falls off the THB-LH

441   and TSS-LH mixing trends (Fig. 10 inset) (Bouquillon et al., 1990; France-Lanord, et al., 1993;

442   Galy and France-Lanord, 1999; Galy et al., 1999; Galy et al., 2010; Lupker et al., 2013;

443   Robinson et al., 2001; Singh et al., 2008). Furthermore, Himalayan terrains have a unique Sr and

444   Nd isotopic signature as compared to other potential sediment sources to the BoB (*e.g.,* Galy et

445   al., 2010). Given the quasi-exclusive G-B sediment source to the BoB channel-levee system, Sr

446   and Nd isotopic data are expected to approximate a multi-member mixing model, reflecting

447   changes in sediment provenance and, hence, erosion distribution within the Himalayan range

448   through time. Thus, assuming transport and delivery mechanisms of sediment from the G-B

449   mouth to the BoB channel-levee system have remained constant with respect to the transference

450   of Sr and Nd isotopic signatures, these proxies can be used to track relative changes in Bengal

451   Fan sediment provenance through time (at least since deglaciation).

452   Several records have demonstrated that, following the LG and into the early Holocene,

453   enhanced erosion in the High Himalayas increased sediment export — notably that derived from

454   HHC and LH terranes — to the coast (*e.g.*, Bookhagen et al., 2005; Clift et al., 2008; Goodbred

455   and Kuehl, 2000). However, other post-glacial provenance reconstructions from the upper BoB

456   channel-levee system indicated that the balance between sediment derived from various

457   Himalayan terranes has remained relatively stable and consistent with modern mixing (Galy et

458   al., 2008a; Lupker et al., 2013; Pierson-Wickmann et al., 2001). Our data present the first record

459   from which paleo-precipitation and provenance and weathering proxies are derived from the

460   same sediments. While the HHC remains the dominant source of sediment (akin to the modern

461   G-B river system), these records — particularly ^{87}Sr/^{86}Sr compositions (Figs 4c, 9j), which are

462   less sensitive to hemipelagic contributions than εNd values — reveal small to moderate source

463   variations through time. Specifically, during warmer, wetter periods — as reflected by δD_p — Sr

464   and Nd isotope compositions reflect roughly equivalent mixing between LH (Himalaya Front

465   Range) and THB (Tibetan Plateau) sources and enhanced contribution of sediment from the

466   HHC (located between the LH and THB terranes; see Fig. 1b), whereas during cooler, drier

467   periods, there is relatively enhanced THB and/or TSS sourcing, at the expense of HHC and LH

468   contributions (Figs. 9, 10). A single outlier at 13.6 ka (Bølling-Allerød) is likewise highly

469   depleted in deuterium and ^{13}C and has a sediment Sr and Nd isotopic composition which closely

470   approximates THB-dominated THB/LH/HHC mixing, again suggesting that this sample may

471   capture a large discharge event from the THB-dominated upper Brahmaputra / Tsangpo drainage

472   basin.

473   Among a range of possible explanations for this subtle post-glacial correlation between

474   climate and sediment provenance, several are most likely given observed trends. Following the

475   LG, meltwater (loaded with OC-poor, mechanically eroded glacial flour) from more expansive

476   glaciers across the high-elevation TSS (see location, Fig. 1b) may have contributed more to the

477   water discharge, especially given lower overall discharge associated with a relatively weak ISM,

478   thereby providing for relatively enhanced export of TSS-derived sediment. Such a scenario

479   would account for the relatively low degree of chemical weathering observed in BoB channel

480   levee sediments deposited during periods of enhanced export during the latest Pleistocene to

481   early Holocene. Moreover, this sediment would have been relatively OC-depleted, allowing for

482   acquisition of OC, and its attendant isotopic signatures, during its transit through the floodplain.

483   Alternatively (or additionally), strengthening of the ISM during the late Pleistocene and early

484   Holocene led to focusing of rainfall on the HHC and LH. Enhanced rainfall on land recently

485   exposed by shrinking glaciers in the high elevation HHC removed large volumes of

486   mechanically eroded, glacially liberated sediment from this system, enhancing HHC

487   contributions to overall G-B sediment discharge. This would have been at the relative expense of

488   the THB and/or TSS, a process observed over shorter time periods (Bookhagen et al., 2005).

489   This hypothesis is supported by Clift et al. (2008) who found that, although ISM strength closely

490   controls erosion rates in both the LH and HHC, the effect was larger for the southerly LH. Thus,

491   Sr and Nd provenance proxy shifts may indicate enhanced precipitation focusing on the

492   Himalayan Front Range and decreased meltwater contributions, and not (only) an increase in

493   sediment export from formerly glaciated regions of the High Himalayas.

494

495   *5.3. Controls on post-glacial organic carbon burial in the Bengal Fan*

496   Despite being organic-poor (average: < 0.5% OC; Galy et al., 2007), the enormous

497   sediment volume from the G-B rivers leads to a terrestrial biospheric OC burial flux of ~3.9 x

498   10^{11} mol/yr, that is *ca.* 20% of the modern global total (Galy et al., 2007, 2011). This is also

499   sustained by high burial efficiency; that is, the modern G-B rivers retain consistent OC loads

500   through burial in the Bengal Fan (Galy et al., 2007). Our data reveal that, despite substantial

501   changes in paleohumidity (section 5.1.1), vegetation composition (5.1.2), and monsoon focusing

502   (section 5.2) over the last 18,000 years, sediment OC loading in the Bengal Fan has remained

503   roughly constant and within 35% of modern values since the LG (Fig. 5b). Temporal changes in

504   OC burial rates at the middle Bengal Fan channel-levee system during this time are thus

505   controlled predominantly by changes in sediment discharge and burial rates.

506   Carbon-export and burial rates are also independent of the degree of chemical weathering

507   of these same sediments (see section 4.2 and Supplemental Fig. 9): assuming K/Si*, Ca/Si,

508   detrital carbonate content, and H_2O^+/Si^* ratios are indeed valid proxies for the degree of

509   chemical weathering at the catchment scale, weathering intensity increases gradually and

510   unidirectionally through time. By contrast, OC* values remain within a narrow range and show

511   no temporal trend. Thus, we conclude that, whereas OC loading is independent of climate, the

512   export and burial of OC in the BoB primarily reflects sediment export and burial rates – and thus

513   terrestrial *physical* erosion rates –since the LG. This outcome is in line with recent findings for

514   the modern global fluvial carbon export (Galy et al., 2015). In the G-B basin, this erosion /

515   carbon-sequestration coupling is modulated by climate-geomorphological interactions in

516   response to, for example, precipitation amount, rainfall, and erosion focusing.

517   By contrast, the final depocenter – and thus the rate and depth of burial – of this OC is

518   controlled by river, shelf, and slope sediment transport processes. At lower stands of sea level

519   associated with the LG, the confluent G-B river discharged directly into the SoNG and from

520   there directly conveyed sediment and OC to the Bengal Fan (Kuehl et al., 2005), including to the

521   channel-levee system of the middle fan. Following the Younger Dryas, rapid sea-level rise

522   resulted in the flooding of the shelf, severing of the direct connection between the G-B rivers and

523   the SoNG, trapping of sediment on the flooded Bengal margin, and the onset of widespread

524   subaerial and subaqueous delta aggradation (Goodbred and Kuehl, 2000; Weber et al., 1997).

525   Nonetheless, the levee system continued to receive sediment and OC throughout the Holocene,

526   as evidenced by continued accumulation at rates of 20–60 cm/kyr. In fact, unlike many of the

527   large modern fans (*e.g.*, Mississippi, Amazon, Rhone, Indus), the continued, rapid transfer of

528   sediment from the G-B rivers to the head of the SoNG has allowed the Bengal Fan to continue to

529   develop and bury large volumes of OC during the present highstand (Weber et al., 1997).

530

531   **6. Summary and Conclusions**

532   This study presents the first post-glacial paleo-precipitation and paleo-vegetation records

533   from the G-B basin. Our records generally confirm trends observed by earlier regional studies of

534   ISM evolution: during the late glacial, reduced differential heating between the Indian Ocean and

535   the Asian continent weakened summer circulation and produced cooler, drier conditions over the

536   northern BoB, Indo-Gangetic plain and across the Himalaya. Increasing NH insolation during

537   deglaciation and through the mid-Holocene corresponded with an increase in atmospheric CO_2

538   concentrations, mean effective moisture, and monsoonal activity, and a large decline of C4

539   plants, in the G-B basin. Our data also compare favorably with earlier records in their ability to

540   capture shorter-term variability in precipitation and vegetation dominance associated with, *e.g.*,

541   the H1, Bølling-Allerød, and Younger Dryas. Our data do, however, demonstrate a larger

542   amplitude of variation than seen in earlier studies (Contreras-Rosales et al., 2014), possibly

543   reflecting the pure G-B signal transferred to the BoB channel-levee system – as opposed to the

544   mixed sources for the Eastern Bengal Slope (Contreras-Rosales et al., 2016; see supplemental

545   materials for complete discussion) – and the likelihood of contributions from outside the G-B

546   basin to the BoB slope and shelf.

547   In contrast to earlier studies, we find that these climate changes have resulted in notable

548   variations in source contributions to integrated G-B basin sediment export. Specifically, a

549   combination of availability of glacially liberated sediment and monsoon-driven rainfall focusing

550   may have led to higher rates of export from HHC and LH terranes during the recorded period of

551   greatest monsoon strength during latest Pleistocene and early Holocene. In contrast, sediment

552   delivered to the BoB during colder and drier periods (as recorded in concurrent paleoclimate and

553   paleovegetation records) following the LG has a provenance signature suggestive of reduced

554   export from the LH terrane in the South flank of the range. These findings – though not

555   conclusive with regard to responsible mechanisms for observed provenance changes – together

556   highlight the importance and utility of developing concurrent records of paleo-environmental

557   changes and sediment provenance.

558   Finally, despite significant changes in climate, sediment provenance, and transport

559   mechanisms of sediment and organic matter from the G-B river mouth to its depocenter in the

560   middle Bengal Fan since the LG, we demonstrate that carbon loading – and thus sediment-

561   volume and grain-size- normalized burial rates – has remained within the narrow range of the

562   modern rivers through time. Burial rates respond almost exclusively to sediment deposition rates,

563   which are in turn largely controlled by monsoon strength and sea level. In contrast, variations in

564   the degree of chemical weathering of sediment exported by the G-B rivers do not follow climate

565   variations in a straightforward manner, as previously observed over longer timescales (Wilson et

566   al., 2015), thus demonstrating the possible late Holocene decoupling of climate forcing and

567   silicate weathering in the Himalayas. These findings reveal the primacy of physical erosion (as

568   opposed to chemical weathering) and sediment transport mechanisms – modulated by climate

569   variability, monsoon focusing, and sea-level change following deglaciation – in controlling

570   sediment / OC export from G-B system, and thus the burial and sequestration of OC within the

571   BoB marine archive. These outcomes together demonstrate a closer coupling between post-

572   glacial variations in monsoon strength and OC burial than between changes in monsoon strength

573   and silicate weathering, and further highlight the potential importance of climatic controls on

574 physical processes within the G-B system — and more broadly other highly erosive systems —

575 in the medium-term (glacial-interglacial) global carbon cycle.

576

583

584 **8. References**

585 Blaauw, M., 2010. Methods and code for 'classical' age-modelling of radiocarbon sequences,
586   *Quaternary Geochronology*, v. 5, p.512-518.

587 Blair, N.E. and Aller, R.C., 2012. The fate of terrestrial organic carbon in the marine
588   environment, *Annual Review of Marine Science*, v. 4, p. 401-423.

589 Botsyun, S., Sepulchre, P., Risi, C. and Donnadieu, Y., 2016. Impacts of Tibetan Plateau uplift
590   on atmospheric dynamics and associated precipitation δ^{18}O, *Climate of the Past*, v. 12,
591   p.1401-1420.

592 Bookhagen, B., Thiede, R.C. and Strecker, M.R., 2005. Late Quaternary intensified monsoon
593   phases control landscape evolution in the northwest Himalaya, *Geology*, v. 33, p.149-152.

594 Boos W.R. and Kuang Z., 2010. Dominant control of the South Asian monsoon by orographic
595   insulation versus plateau heating, *Nature*, v. 463, p. 218–223.

596 Bouquillon, A., France-Lanord, C., Michard, A. and Tiercelin, J.J., 1987. Sedimentology and
597   isotopic chemistry of the Bengal Fan sediments: The denudation of the Himalaya. *In:*
598   Cochran, J.R., Stow, D.A.V., Auroux, C., Amano, K., Balson, P.S., Boulégue, J.J., Brass,

26

G.W., Corrigan, J., Gartner, S., Hall, S., Iaccarino, S., Ishizuka, T., Decima, F.P., Raman, C.V., Sager, W.W., Takahasi, K., Thompson, T.L., Tiercelin, J.-J., Townsend, M.R., Wetzel, A., Wijayananda, N.P., and Williams, C. (eds), *Proceedings of the Ocean Drilling Program: Scientific Results Volume 116*, College Station, Texas: Ocean Drilling Program, p. 43-58.

Cheng, H., Edwards, R.L., Sinha, A., Spötl, C., Yi, L., Chen, S., Kelly, M., Kathayat, G., Wang, X., Li, X. and Kong, X., 2016. The Asian monsoon over the past 640,000 years and ice age terminations, *Nature*, v. 534, p.640-646.

Clark, P.U., Dyke, A.S., Shakun, J.D., Carlson, A.E., Clark, J., Wohlfarth, B., Mitrovica, J.X., Hostetler, S.W. and McCabe, A.M., 2009. The last glacial maximum, *Science*, v. 325, p.710-714.

Clemens, S.C., Prell, W.L. and Sun, Y., 2010. Orbital-scale timing and mechanisms driving Late Pleistocene Indo-Asian summer monsoons: Reinterpreting cave speleothem $\delta^{18}O$, *Paleoceanography*, v. 25, PA4207.

Clement, A.C., Cane, M.A. and Seager, R., 2001. An Orbitally Driven Tropical Source for Abrupt Climate Change, *Journal of Climate*, v. 14, p.2369-2375.

Clift, P.D., Giosan, L., Blusztajn, J., Campbell, I.H., Allen, C., Pringle, M., Tabrez, A.R., Danish, M., Rabbani, M.M., Alizai, A. and Carter, A., 2008. Holocene erosion of the Lesser Himalaya triggered by intensified summer monsoon, *Geology*, v. 36, p.79-82.

Colin, C., Turpin, L., Blamart, D., Frank, N., Kissel, C., and Duchamp, S., 2006. Evolution of weathering patterns in the Indo-Burman Ranges over the last 280 kyr: Effects of sediment provenance on $^{87}Sr/^{86}Sr$ ratios tracer, *Geochemistry, Geophysics, Geosystems,* v. 7, Q03007.

Contreras-Rosales, L.A., Jennerjahn, T., Tharammal, T., Meyer, V., Lückge, A., Paul, A., and Schefuß, E., 2014. Evolution of the Indian Summer Monsoon and terrestrial vegetation in the Bengal region during the past 18 ka, *Quaternary Science Reviews*, v. 102, p. 133-148.

623   Contreras-Rosales, L.A., Schefuß, E., Meyer, V., Palamenghi, L., Lückge, A. and Jennerjahn,
624   T.C., 2016. Origin and fate of sedimentary organic matter in the northern Bay of Bengal
625   during the last 18ka, *Global and Planetary Change,* v. 146, p. 53-66.

626   Curray, J.R., Emmel, F.J., and Moore, D.G., 2003. The Bengal Fan: morphology, geometry,
627   stratigraphy, history and processes, *Marine and Petroleum Geology*, v. 19, p. 1191-1223.

628   Fournier, L., Fauquembergue, K., Zaragosi, S., Zorzi, C., Malaizé, B., Bassinot, F., Joussain, R.,
629   Colin, C., Moreno, E., and Leparmentier, F., 2016. The Bengal Fan: External controls on the
630   Holocene Active Channel turbidite activity, *The Holocene*, 0959683616675938.

631   France-Lanord, C., and Derry, L.A., 1997. Organic carbon burial forcing of the carbon cycle
632   from Himalayan erosion, *Nature*, v. 390 p. 65-67.

633   France-Lanord, C., Derry, L. and Michard, A., 1993. Evolution of the Himalaya since Miocene
634   time: isotopic and sedimentological evidence from the Bengal Fan, *Geological Society,*
635   *London, Special Publications*, v. 74, p.603-621.

636   Galy, A. and France-Lanord, C., 1999. Weathering processes in the Ganges–Brahmaputra basin
637   and the riverine alkalinity budget, *Chemical Geology*, v. 159, p.31-60.

638   Galy, A., France-Lanord, C., and Derry, L.A., 1999. The strontium isotopic budget of Himalayan
639   rivers in Nepal and Bangladesh, *Geochimica et Cosmochimica Acta*, v. 63, p. 1905-1925.

640   Galy, V., and Eglinton, T.I., 2011. Protracted storage of biospheric carbon in the Ganges-
641   Brahmaputra basin. *Nature Geoscience,* v. 4, p. 843-847.

642   Galy, V., Eglinton, T., France-Lanord, C., and Sylva, S., 2011. The provenance of vegetation and
643   environmental signatures encoded in vascular plant biomarkers carried by the Ganges-
644   Brahmaputra rivers. *Earth and Planetary Science Letters*, v. 304, p. 1-12.

645   Galy, V., France-Lanord, C., Beyssac, O., Faure, P., Kudrass, H. and Palhol, F., 2007. Efficient
646   organic carbon burial in the Bengal fan sustained by the Himalayan erosional system, *Nature*,
647   v. 450, p.407-410.

648   Galy, V., François, L., France-Lanord, C., Faure, P., Kudrass, H., Palhol, F. and Singh, S.K.,

649   2008a. C4 plants decline in the Himalayan basin since the Last Glacial Maximum,

650   *Quaternary Science Reviews*, v. 27, p.1396-1409.

651   Galy, V., France-Lanord, C. and Lartiges, B., 2008b. Loading and fate of particulate organic

652   carbon from the Himalaya to the Ganga–Brahmaputra delta, *Geochimica et Cosmochimica*

653   *Acta*, v. 72, p.1767-1787.

654   Galy, V., France-Lanord, C., Peucker-Ehrenbrink, B., and Huyghe, P., 2010. Sr-Nd-Os evidence

655   for a stable erosion regime in the Himalaya during the past 12 Myr, *Earth and Planetary*

656   *Science Letters*, v. 290, p. 474-480.

657   Galy, V., Peucker-Ehrenbrink, B. and Eglinton, T., 2015. Global carbon export from the

658   terrestrial biosphere controlled by erosion, *Nature*, v. 521, p. 204-207.

659   Goodbred, S.L., and Kuehl, S.A., 2000. Enormous Ganges-Brahmaputra sediment discharge

660   during strengthened early Holocene monsoon, *Geology*, v. 28, p. 1083-1086.

661   Hedges, J.I., Oades, J.M., 1997. Comparative organic geochemistries of soils and marine

662   sediments, *Organic Geochemistry*, v. 27, p. 319-361.

663   Herzschuh, U., 2006. Palaeo-moisture evolution in monsoonal Central Asia during the last

664   50,000 years, *Quaternary Science Reviews,* v. 25, p. 163-178.

665   Huang, S.Y., Chen, Y.G., Burr, G.S., Jaiswal, M.K., Lin, Y.N., Yin, G., Liu, J., Zhao, S. and

666   Cao, Z., 2014. Late Pleistocene sedimentary history of multiple glacially dammed lake

667   episodes along the Yarlung-Tsangpo river, southeast Tibet. *Quaternary Research*, v. 82,

668   p.430-440.

669   IAEA/WMO (2016). Global Network of Isotopes in Precipitation. The GNIP Database.

670   Accessible at: http://www.iaea.org/water

671   Kudrass, H.R., Hofmann, A., Doose, H., Emeis, K. and Erlenkeuser, H., 2001. Modulation and

672   amplification of climatic changes in the Northern Hemisphere by the Indian summer

673   monsoon during the past 80 ky, *Geology*, v. 29, p.63-66.

674　　　Kuehl, S.A., Levy, B.M., Moore, W.S. and Allison, M.A., 1997. Subaqueous delta of the
675　　　　　Ganges-Brahmaputra river system, *Marine Geology*, v. 144, p.81-96.

676　　　Kuehl, S.A., Allison, M.A., Goodbred, S.L., and Kudrass, H., 2005. The Ganges-Brahmaputra
677　　　　　Delta. *In:* Giosan, L., and Bhattacharya, J.P. (eds), *River Deltas: Concepts, Models and*
678　　　　　*Examples.* Journal of the Society for Sedimentary Geology (SEPM) Special Publication No.
679　　　　　83, p. 413–434,

680　　　Ludwig, W., Amiotte-Suchet, P., Munhoven, G. and Probst, J.L., 1998. Atmospheric CO_2
681　　　　　consumption by continental erosion: Present-day controls and implications for the last glacial
682　　　　　maximum, *Global and Planetary Change*, v. 16, p.107-120.

683　　　Lupker, M., Blard, P.H., Lave, J., France-Lanord, C., Leanni, L., Puchol, N., Charreau, J. and
684　　　　　Bourlès, D., 2012. ^{10}Be-derived Himalayan denudation rates and sediment budgets in the
685　　　　　Ganga basin, *Earth and Planetary Science Letters*, v. 333, p.146-156.

686　　　Lupker, M., France-Lanord, C., Galy, V., Lavé, J. and Kudrass, H., 2013. Increasing chemical
687　　　　　weathering in the Himalayan system since the Last Glacial Maximum, *Earth and Planetary*
688　　　　　*Science Letters*, v. 365, p.243-252.

689　　　Marzin, C., Kallel, N., Kageyama, M., Duplessy, J.C., and Braconnot, P., 2013. Glacial
690　　　　　fluctuations of the Indian monsoon and their relationship with North Atlantic climate: new
691　　　　　data and modelling experiments. *Climate of the Past*, v. 9, p. 2135-2151.

692　　　Pierson-Wickmann, A.-C., Reisberg, L., France-Lanord, C., and Kudrass, H., 2001. Os-Sr-Nd
693　　　　　results from sediments in the Bay of Bengal: Implications for sediment transport and the
694　　　　　marine Os record, *Paleoceanography*, v. 16, p. 435-444.

695　　　Rao, Z., Li, Y., Zhang, J., Jia, G. and Chen, F., 2016. Investigating the long-term palaeoclimatic
696　　　　　controls on the δD and δ^{18}O of precipitation during the Holocene in the Indian and East
697　　　　　Asian monsoonal regions, *Earth-Science Reviews*, v. 159, p.292-305.

698　　　Robinson, D.M., Decelles, P.G., Patchett, P.J., and Garzione, C.N., 2001. The kinematic
699　　　　　evolution of the Nepalese Himalaya interpreted from Nd isotopes, *Earth and Planetary*
700　　　　　*Science Letters*, v. 192, p. 507– 521.

701 Schwenk, T., Spieß, V., Hübscher, C., and Breitzke, M., 2003. Frequent channel avulsions within
702   the active channel–levee system of the middle Bengal Fan—an exceptional channel–levee
703   development derived from Parasound and Hydrosweep data, *Deep Sea Research Part II:*
704   *Topical Studies in Oceanography*, v. 50, p.1023-1045.

705 Severinghaus, J.P., Beaudette, R., Headly, M.A., Taylor, K. and Brook, E.J., 2009. Oxygen-18 of
706   O2 records the impact of abrupt climate change on the terrestrial biosphere. Science,
707   324(5933), pp.1431-1434.

708 Singh, S., Rai, S., Krishnaswami, S., 2008. Sr and Nd isotopes in river sediments from the Ganga
709   Basin: Sediment provenance and spatial variability in physical erosion, *Journal of*
710   *Geophysical Research*, v. 113, F03006.

711 Vernekar, A.D., Zhou, J., Shukla, J., 1995. The effect of Eurasian snow cover on the Indian
712   monsoon, *Journal of Climate*, v. 8, p. 248–266.

713 Weber, M.E., Wiedicke, M.H., Kudrass, H.R., Hübscher, C., and Erlenkeuser, H., 1997. Active
714   growth of the Bengal Fan during sea-level rise and highstand, *Geology*, v. 25, p. 315-318.

715 West, A.J., Galy, A. and Bickle, M., 2005. Tectonic and climatic controls on silicate weathering,
716   *Earth and Planetary Science Letters*, v. 235, p.211-228.

717 Wilson, D.J., Galy, A., Piotrowski, A.M. and Banakar, V.K., 2015. Quaternary climate
718   modulation of Pb isotopes in the deep Indian Ocean linked to the Himalayan chemical
719   weathering, *Earth and Planetary Science Letters*, v. 424, p.256-268.

720 Wu, G.X., Liu, Y., He, B., Bao, Q., Duan, A., and Jin, F.-F., 2012. Thermal controls on the
721   Asian summer monsoon. *Scientific Reports*, v. 2, p. 404.
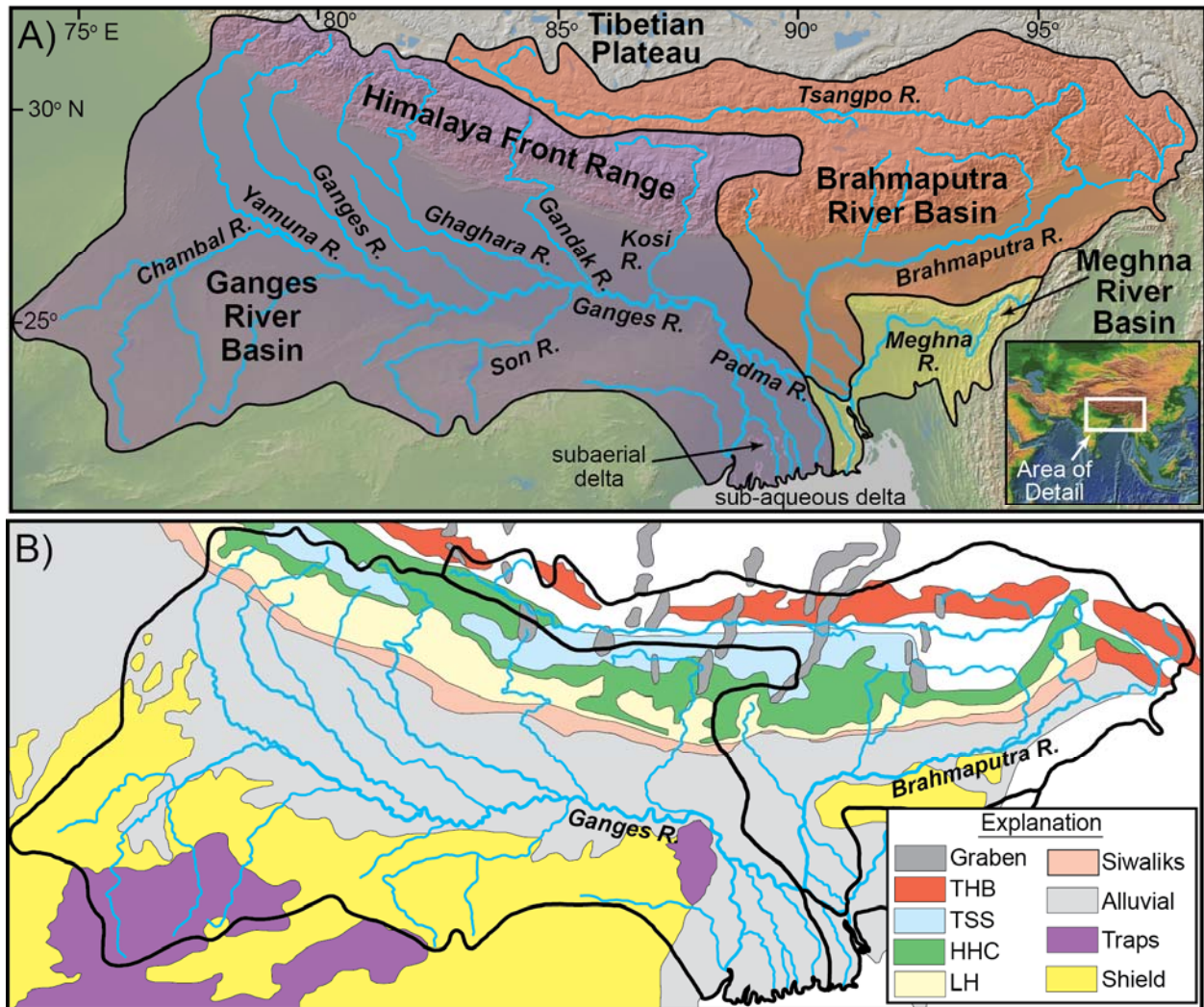
Figures and Tables

Figure 1. (a) Major features and tributaries of the Ganges-Brahmaputra (G-B) drainage basin.

Background topographic image from GeoMapApp. (b) Geologic map of the G-B basin showing

locations of the major terranes (modified from Galy et al., 2010). THB: Trans-Himalaya

Batholith, TSS: Thetisian Sedimentary Series, HHC: High Himalaya Crystalline, LH: Lesser

Himalaya.

730
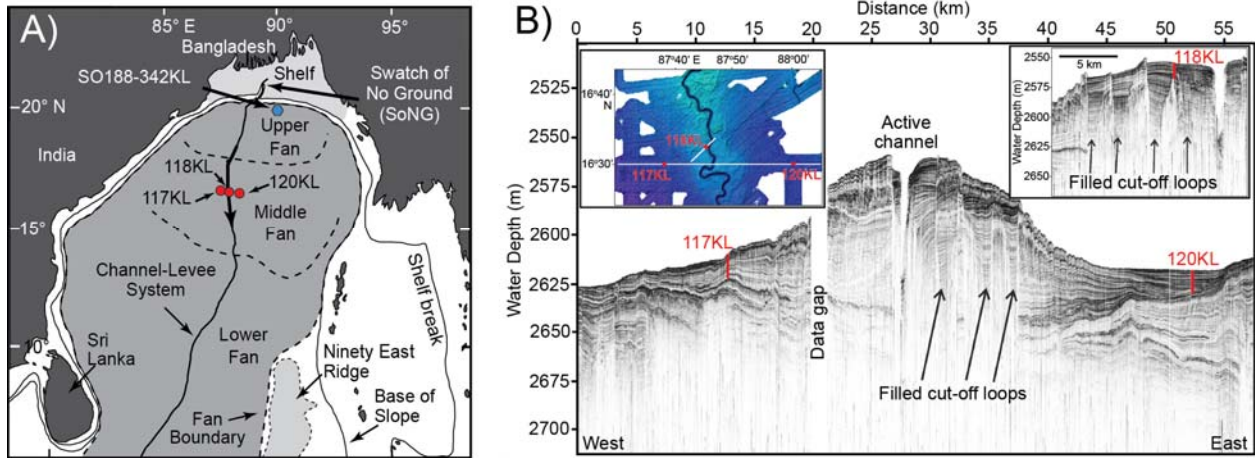
Figure 2. (a) Morphology of the Bengal Fan. Sediment is dominantly delivered via turbidity

currents that travel along single-channel channel-levee system. Red circles: locations of 3 cores

proposed for use in this study (Kudrass, 1996); blue circle: location of core SO188-342KL

(Contreras-Rosales et al., 2014, 2016). (b) Parasound seismic-reflection profile crossing cores

SO93- 117KL and 120KL from west to east. Upper left inset shows locations of the profile and

cores with respect to the pathway of the active channel imaged by multibeam bathymetry. Upper

right inlet shows Parasound data around Core SO93-118 KL, which is located 5 km to the north.

These data reveal the typical architecture of a channel-levee system built by turbidity currents

with a gull-wing shape and reflections diverging within the levee towards the channel. Both

levees show sediment waves resulting from the overspilling turbidity currents. The system can be

separated into undisturbed outer levees surrounding the inner area consisting of the active

channel and filled cut-off loops, as described in detail by Schwenk et al. (2003).

743
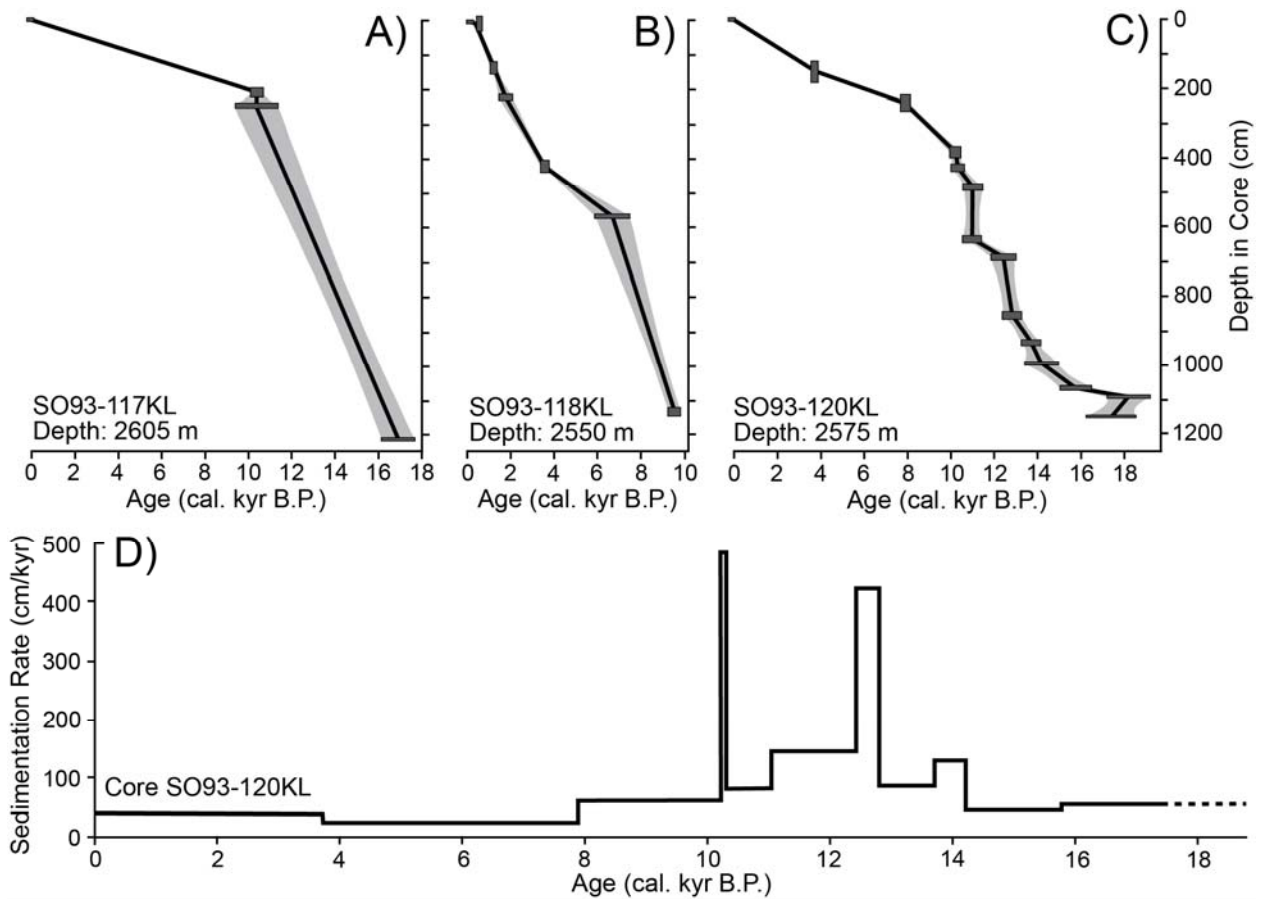
Figure 3. Age models for Bengal Fan channel-levee cores (a) SO93-117KL; (b) SO93-118KL; and (c) SO93-120KL, derived through linear interpolation between calibrated Δ^{14}C ages (Table 1) and extrapolation to core tops and bottoms. Box widths represent sample depth interval within core; heights represent calibrated age error. (d) Linear sedimentation rates calculated from published and new age control points based on core SO93-120KL, the core with the highest-resolution age model.
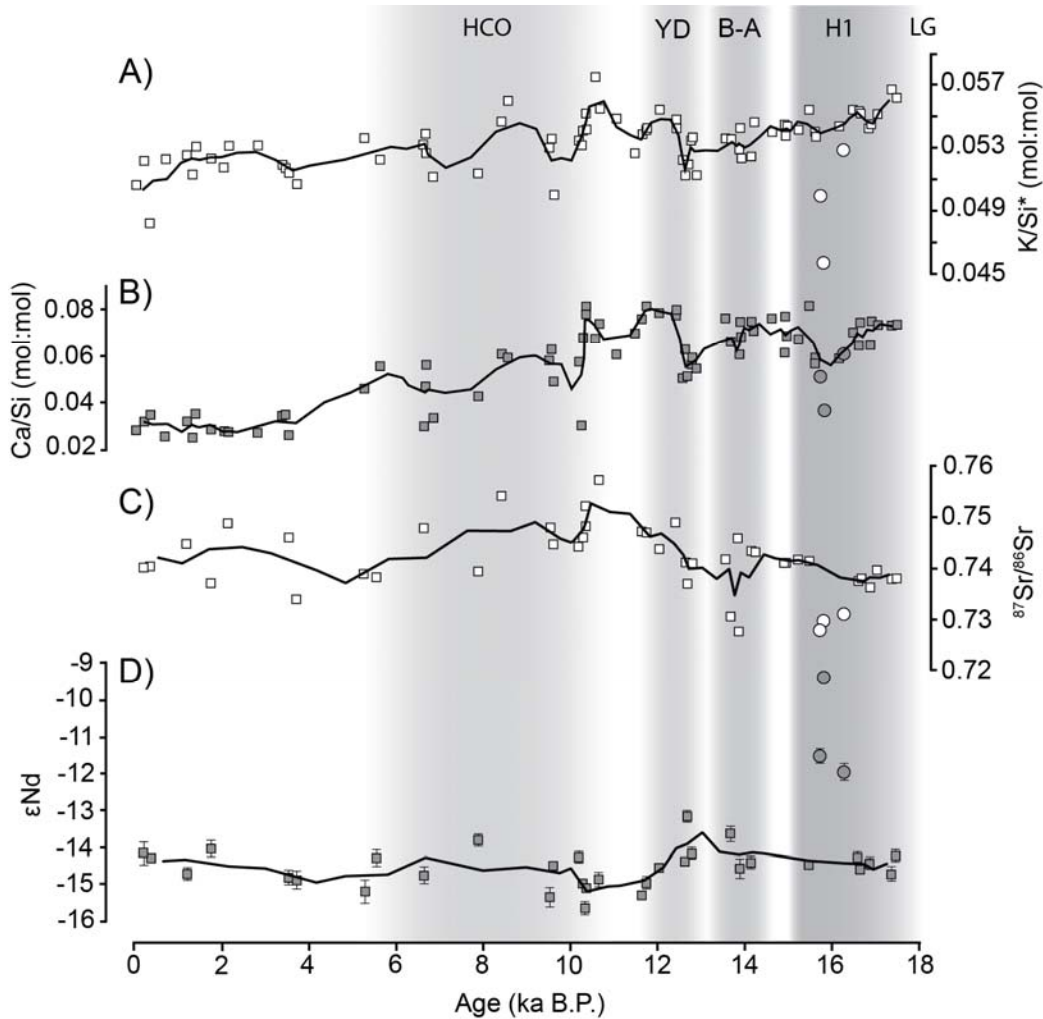
Figure 4. Temporal records of weathering (K/Si* [a]; Ca/Si [b]) and sediment source (strontium [c] and [d] neodymium stable isotopic compositions) from BoB channel levee cores SO93-117KL, -118KL, and -120KL. Data are from Galy et al. (2008a), Galy et al. (2014), Lupker et al. (2013), Pierson-Wickman et al. (2001), and this study. εNd data are from Pierson-Wickman et al. (2001) and this study only. Lines are three-point moving averages. Data points shown as circles at *ca.* 16 ka in all graphs are identified as outliers due to non-negligible hemipelagic influence.

758
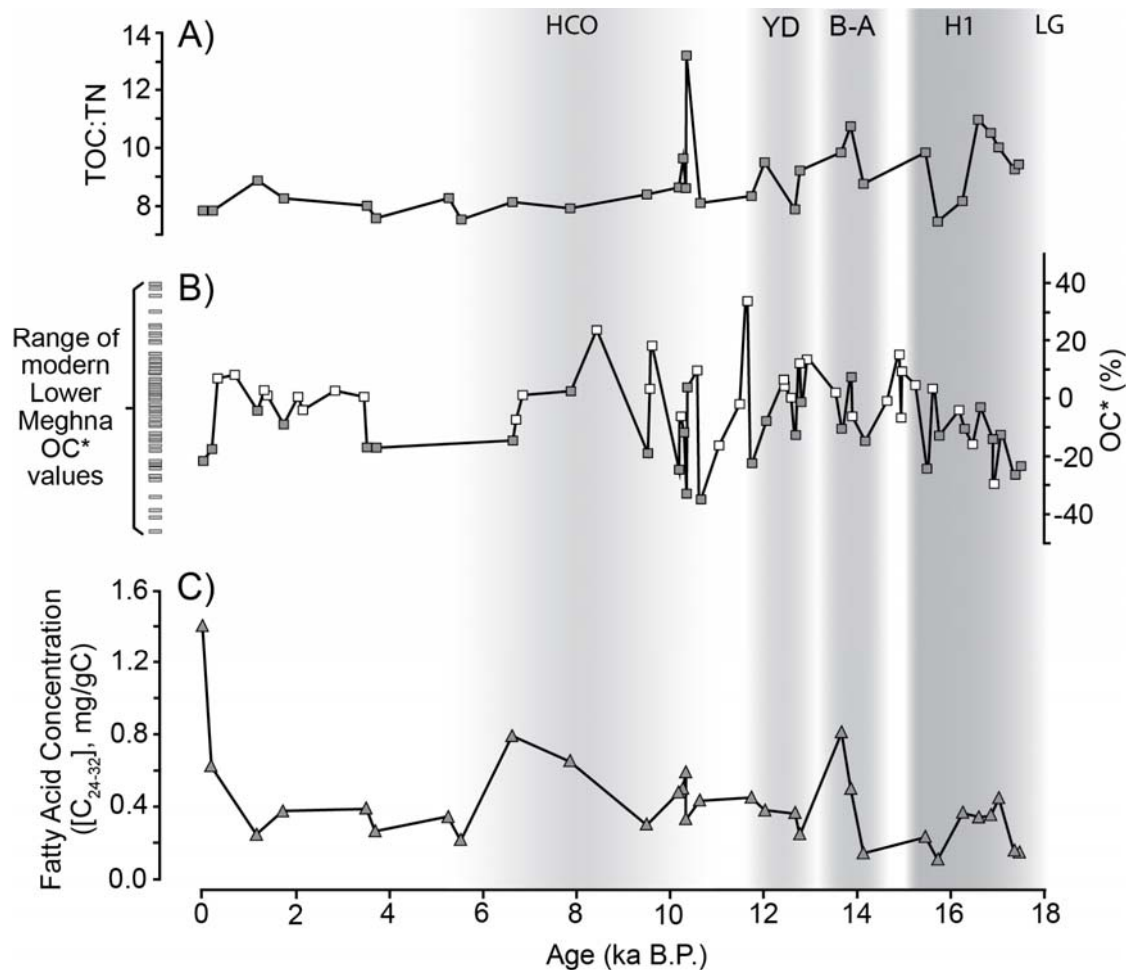
Figure 5. G-B river and BoB channel levee (cores SO93-117KL, -118KL, and -120KL) temporal

760   records of (a) bulk sediment TOC:TN ratios; (b) OC*, the bulk sediment TOC, normalized to

761   Al/Si ratios according to TOC sample preparation method (liquid acidification [open symbols;

762   Galy et al., 2008] vs. fumigation [closed symbols; this study]; see supplemental materials for

763   details), with respect to the modern Lower Meghna River and (c) Concentration of C_{24-32} FA,

764   given as a proxy for terrestrial OC, as a function of bulk sediment OC content. River data in (b)

765   are from Galy et al. (2008b) and three outliers (OC* = 58–103% of modern rivers; data included

766   in Supplemental Table 2) are omitted from (b) due to likely inclusion of marine OC

767   (hemipelagic) or terrestrial vegetation debris.
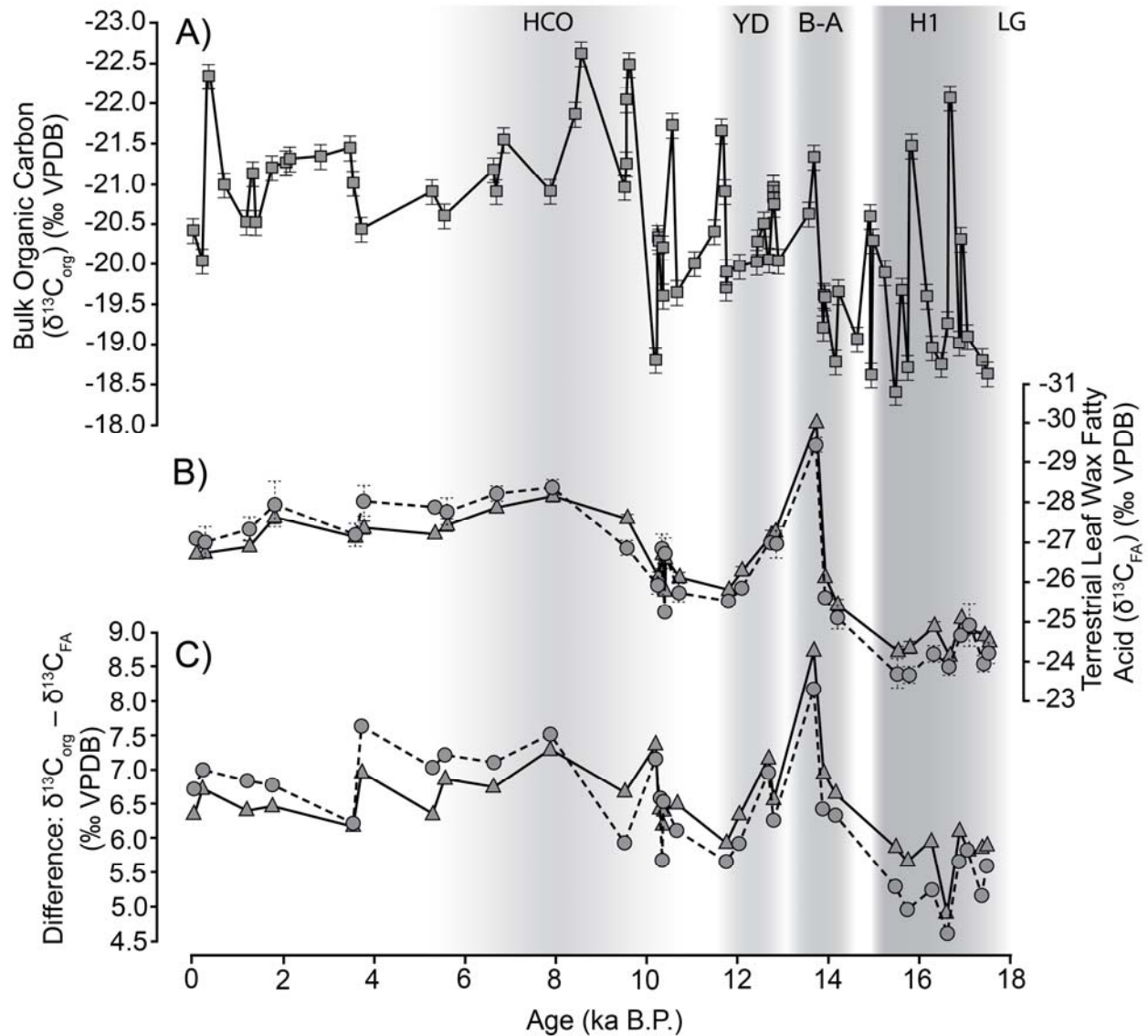
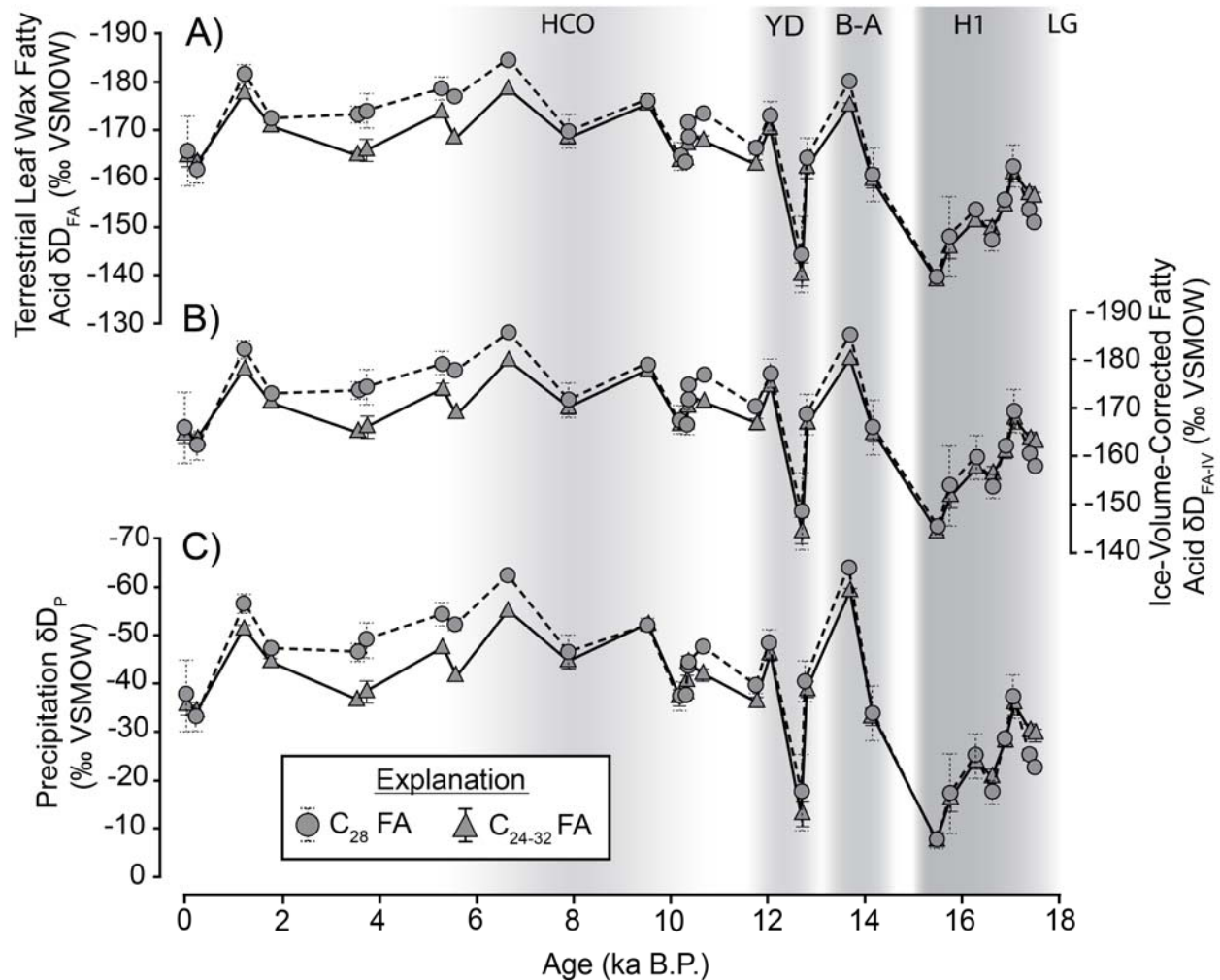**Figure 6.** Temporal evolution of stable carbon isotopic compositions of sediments and leaf wax fatty acids from BoB channel levee cores SO93-117KL, -118KL, and -120KL (this study only). (a) Bulk sediment $\delta^{13}C_{org}$ values; (b) Compound-specific $\delta^{13}C_{FA}$ values for C_{24-32} (triangles) and C_{28} (circles) FAMES. (c) Difference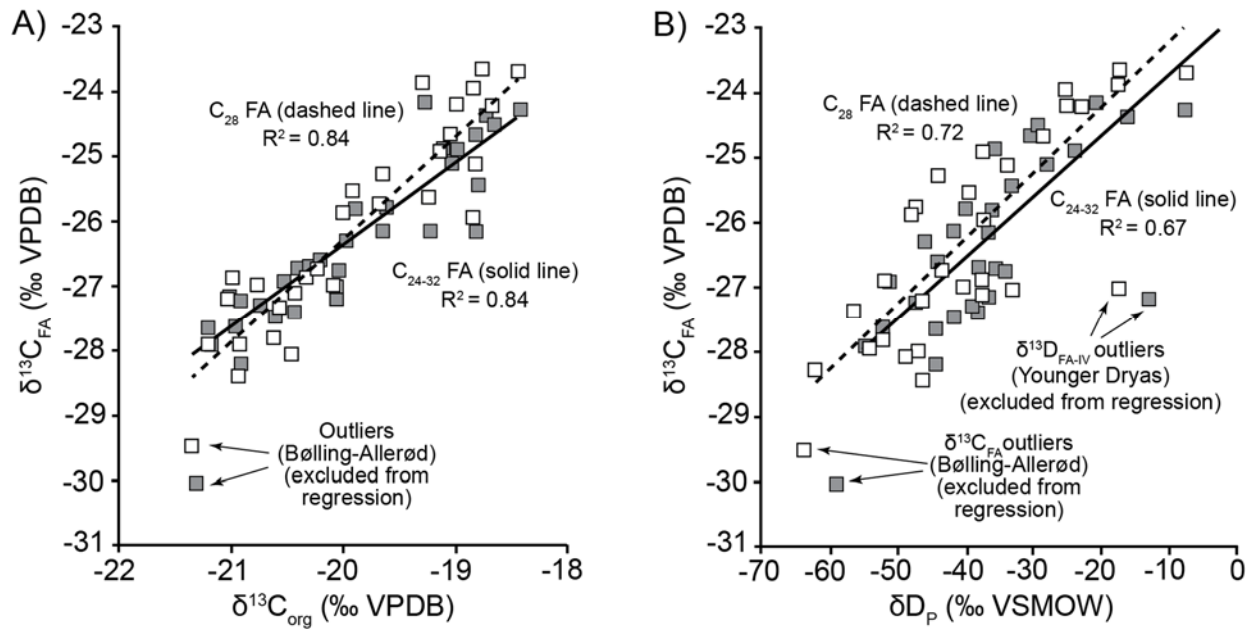 between compound-specific $\delta^{13}C_{FA}$ values for C_{24-32} (triangles) and C_{28} (circles) FAMES and bulk sediment $\delta^{13}C_{org}$ values. Errors are within data points where error bars not shown.

Figure 7. Temporal evolution of stable hydrogen isotopic compositions of leaf wax fatty acids and G-B basin precipitation derived from BoB channel levee cores SO93-117KL, -118KL, and -120KL. (a) Methanol-corrected compound-specific δD_{FA} values for C_{24-32} (triangles) and C_{28} (circles) leaf wax fatty acids. (b) C_{24-32} (triangles) and C_{28} (circles) leaf wax fatty δD_{FA} values corrected for ice-volume effects. (c) Precipitation δD_P values calculated from ice-volume-corrected leaf wax fatty δD_{FA-IV} and basin-integrated vegetation compositions inferred from $\delta^{13}C_{FA}$ values. Errors are within data points where error bars not shown.

Figure 8. Stable isotopic compositions of sediments and FAMES from BoB channel-levee cores SO93-117KL, -118KL, and -120KL. (a) Comparison of bulk $\delta^{13}C_{org}$ values and compound–specific $\delta^{13}C_{FA}$ values for C_{24-32} (filled symbols) and C_{28} (open symbols) leaf wax fatty acids. (a) Comparison of compound-specific $\delta^{13}C_{FA}$ and δD_P values for C_{24-32} (filled symbols) and C_{28} (open symbols) leaf wax fatty acids.

789

40
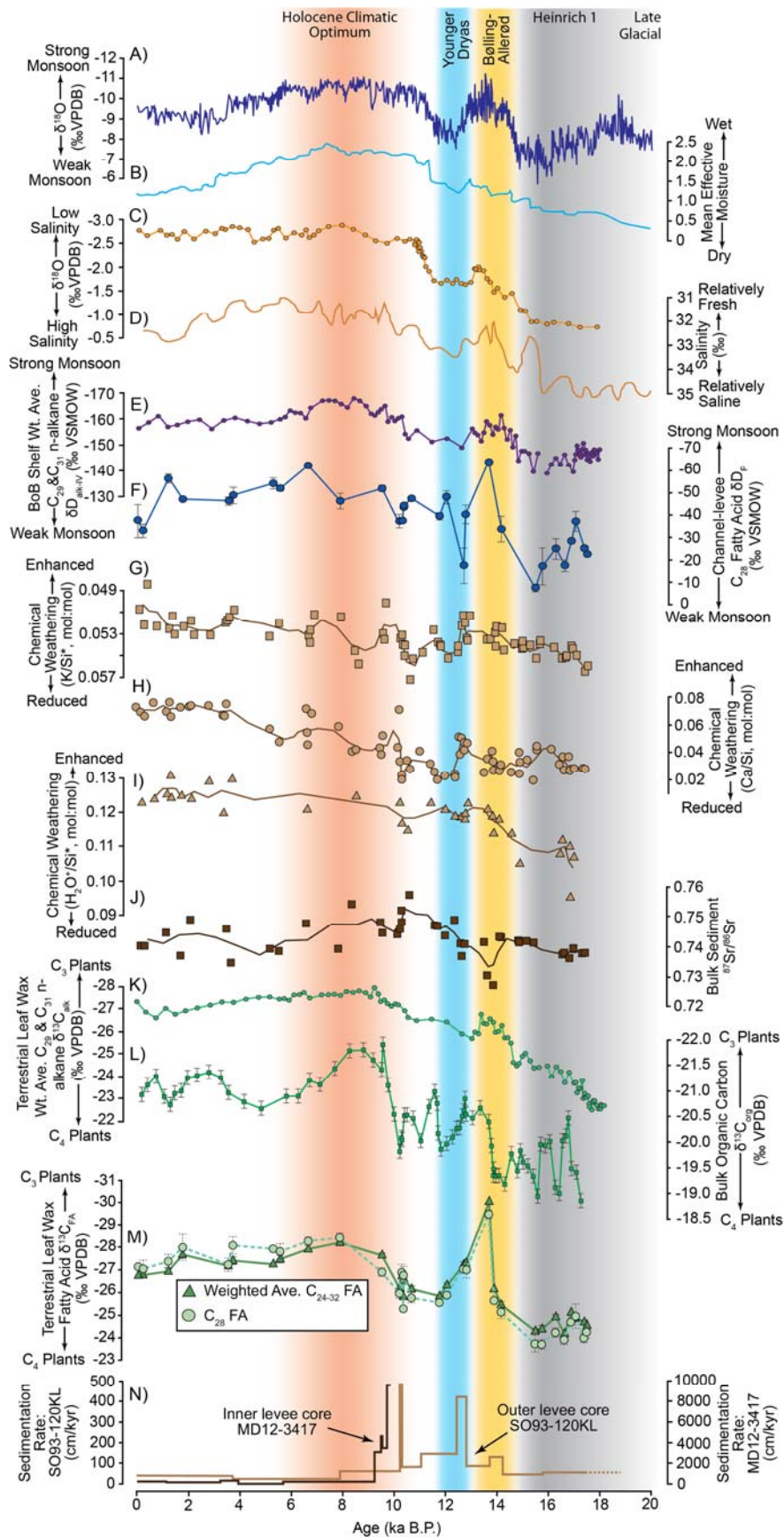
790   *Figure 9.* Comparison on summer monsoon records and records of response in the G-B basin

791   and BoB following the last glacial maximum. (a) Composite Chinese cave speleothem $\delta^{18}O$

792   record (Cheng et al., 2016); (b) mean effective moisture in central Asia (Herzschuh, 2006); (c)

793   three-point moving average of $\delta^{18}O$ of planktonic foraminifers (G. ruber) from BoB channel-

794   levee cores (SO93-117KL, -118KL, and -120KL) (data from Galy et al. [2008a] and Weber et al.

795   [1997]); (d) BoB sea-surface salinity, as derived from foraminifera $\delta^{18}O$ records (Kudrass et al.,

796   2001); (e) ice-volume-corrected compound-specific hydrogen isotope compositions (δD_{ALK-IV}) of

797   plant wax n-alkanes from Bengal Shelf core SO188-342KL (Fig. 2a), sourced from likely mix of

798   G-B basin and Indo-Burman (I-B) range (Contreras-Rosales et al., 2014); (f) ice-volume- and

799   vegetation-fractionation- corrected fatty acid δD_P values from channel-levee cores, sourced

800   solely from G-B basin (this study; see Fig. 7c); (g) data and three-point moving average of

801   terrestrial chemical weathering proxy record (K/Si*; see Fig. 4a); (h) data and three-point

802   moving average of terrestrial chemical weathering proxy record (Ca/Si; see Fig. 4b); (i) data and

803   three-point moving average of sediment hydration, a proxy for terrestrial chemical weathering,

804   from the BoB channel-levee system (Lupker et al., 2013); (j) data and three-point moving

805   average of sediment source proxy record from the BoB channel-levee system ($^{87}Sr/^{86}Sr$; see Fig.

806   4c); (k) compound-specific $\delta^{13}C_{ALK}$ compositions (vegetation type sources) of plant wax n-

807   alkanes from Bengal Shelf core SO188-342KL (Contreras-Rosales et al., 2014); (l) 3-pt. moving

808   average of bulk $\delta^{13}C_{org}$ channel-levee cores (data from Galy et al. [2008a], Galy et al. [2014],

809   and this study); (m) compound-specific $\delta^{13}C_{FA}$ compositions of plant wax n-alkanoic (fatty)

810   acids from channel-levee cores (this study; see Fig. 6b); (n) sedimentation rate for outer channel-

811   levee core SO93-120KL (this study) and inner levee core MD12-3416 (Fournier et al., 2016).
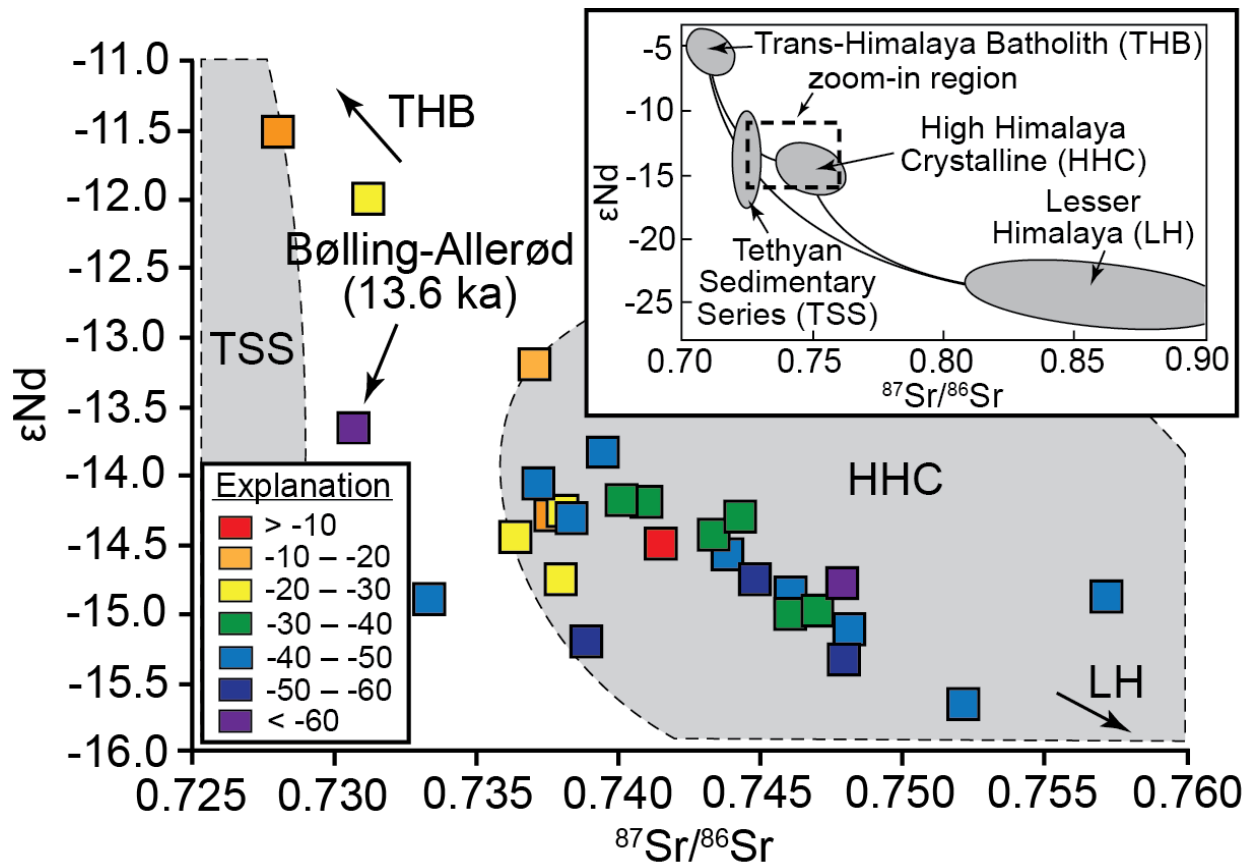
Figure 10. Sr–Nd isotope mixing plot of sediments from BoB channel-levee cores SO93-117KL, -118KL, and -120KL (this study only), color-coded by precipitation δD_P values calculated from leaf-wax fatty acid δD_{FA-IV} values derived from those same samples. Note that εNd values of two most enriched samples (upper left) likely have some contribution from hemipelagic sediments (see Supplemental Fig. 6). Inset: Sr–Nd isotope mixing plot showing the major lithologic units of the Himalayan range (inset modified from Galy et al. [2010]; TSS data field are from Bouquillon et al. [1990], France-Lanord, et al. [1993], Galy and France-Lanord [1999], and Robinson et al. [2001]).